Icarus 338 (2020) 113473

Contents lists available at ScienceDirect

Icarus

journal homepage: www.elsevier.com/locate/icarus

The spectroscopic properties of the Lixiaohua family, cradle of Main Belt Comets

M.N. De Prá [a,b,*], J. Licandro [c,d], N. Pinilla-Alonso [a], V. Lorenzi [e,c], E. Rondón [b], J. Carvano [b], D. Morate [b], J. De León [c,d]

[a] Florida Space Institute, University of Central Florida, FL, USA
[b] Departamento de Astrofísica, Observatório Nacional, Rio de Janeiro, 20921-400, Brazil
[c] Instituto de Astrofísica de Canarias, C/Vía Láctea s/n, 38205 La Laguna, Spain
[d] Departamento de Astrofísica, Universidad de La Laguna, 38206 La Laguna, Tenerife, Spain
[e] Fundación Galileo Galilei - INAF, 38712 Breña Baja, Tenerife, Spain

ARTICLE INFO

Keywords:
Asteroids

ABSTRACT

The Lixiaohua collisional family lies in the Outer Main Belt, close to the well characterized Themis primitive class family. It is one of the only three families that host two active asteroids that present cometary-like activity: 313P/Gibbs and 358P/PANSTARRS (P/2012 T1). As a part of the PRIMitive Asteroid Spectroscopy Survey (PRIMASS), we present the results of a spectroscopic program where we acquired 36 objects in visible wavelengths, using the 4.1 m SOAR, and, 17 objects in the near-infrared, using the 3.58 m Telescopio Nazionale Galileo, which provided the characterization of 43 out of the 756 identified Lixiaohua family members. We observed asteroids members of the Lixiaohua family with the aim of: (1) determining the spectral class and spectroscopic properties of the family, (2) estimating the presence of hydrated minerals on their surfaces by studying the 0.7 μm absorption band and the UV drop of reflectance below 0.5 μm, (3) analyzing if active asteroids 358P and 313P are probable family members. Our results show that the Lixiaohua family is consistently redder families than the Themis family and present a wide variety of slopes. We have not found an unambiguous trace of aqueous alteration in the spectra of the family members, at the observed wavelengths. Finally, we conclude that the Lixiaohua family is the probable source of the Main-Belt Comets 313P/Gibbs and 358P/PANSTARRS.

1. Introduction

Active Asteroids (AAs) are small bodies with orbits typical of asteroids ($T_J > 3.00$) that exhibit cometary activity. There are several mechanisms that can trigger activity in an asteroid (Jewitt, 2012), such as an impact, rotational break-up, thermal fracturing or sublimation of volatiles. Objects in the Main-Belt, in which the activity is believed to be driven by sublimation of ices are also referred to as Main-Belt Comets (MBC) (Jewitt, 2012; Jewitt et al., 2015b). This latter group has attracted considerable attention in the last years, since they are believed to have formed close to their in-situ location (Haghighipour, 2009; Hsieh and Haghighipour, 2016) and can be considered a probe to the volatile content hidden in the Main-Belt.

The discovery of water ice in the main-belt, indirectly through MBC, and directly in the surface of (24) Themis, (65) Cybele and (1) Ceres (Campins et al., 2010; Rivkin and Emery, 2010; Licandro et al., 2011; Platz et al., 2016) are specially interesting for Solar System and Earth formation models. These objects can help constrain the thermal and dynamical history of the Solar System, and where primitive asteroids were actually formed. Also, there are modern theories that propose that Earth's water were accreted from collisions with volatile-rich bodies, most likely originating from the asteroid belt (Morbidelli et al., 2000).

The relation of AAs with collisional families is not considered to be uncommon. In fact, there are three AAs related to the old Themis family. In addition, a fourth object, 238P/Read, could be a escaped Themis family member (Haghighipour, 2009). The Lixiaohua family lies in the outer main belt, at semi-major axis ~ 3.11 au, close to the well studied Themis family, but at higher eccentricity and inclination (Nesvorný et al., 2015). Recent works have attributed two Active Asteroids (AAs) as members of the family: 313P/Gibbs and 358P/PANSTARRS (P/2012 T1) (Hsieh et al., 2013, 2018b). In addition, the work of Hsieh et al. (2018b) provides possible links for another AAs belonging to other

* Correspondence to: Florida Space Institute, University of Central Florida, Partnership I, Research Pkwy, 32826, Orlando, FL, USA.
E-mail address: mariodepra@ucf.edu (M.N. De Prá).

https://doi.org/10.1016/j.icarus.2019.113473
Received 1 July 2019; Received in revised form 7 October 2019; Accepted 10 October 2019
Available online 31 October 2019

families, most of them located in the outer main-belt. In this context, the study of the collisional families that host Main Belt Comets is of fundamental importance to understand their activation mechanisms and the abundance of water in the parental bodies.

The object 358P/PANSTARRS (hereafter 358P) was originally discovered active in October of 2012, while 313P/Gibbs (hereafter 313P) was discovered in September 2014. Follow up observations showed that the slow brightness variation and coma morphology of these objects were probably caused by a prolonged activity rather than by a single event, compatible with a sublimation driven activity (Moreno et al., 2013; Hsieh et al., 2013; Jewitt et al., 2015a; Hsieh et al., 2015).

A strong indicative of a sublimation-driven coma is the recurrent activity when the objects are near to their perihelion. This behavior was detected in both MBCs. The object 313P was observed active in precovery images from 2003 of the Sloan Digital Sky Survey (SDSS) (Hsieh et al., 2015; Hui and Jewitt, 2015). Agarwal and Mommert (2018) observed 358P on July and August, 2017, at heliocentric distance of ~ 2.741, seven months before the object reached perihelion, and found that activity was not detectable at that distance. Recently, Hsieh et al. (2018a) presented new images of 358P with recurrent active on November, 2017, at heliocentric distance < 2.522.

There were several attempts to measure gas emission on 313P and 358P, through spectroscopic observations at near-ultraviolet wavelengths (Hsieh et al., 2013; Jewitt et al., 2015a; Snodgrass et al., 2017; O'Rourke et al., 2013). Although emission bands were never detected, these works could establish upper limits for the gas production rate. At present date, direct gas emission detection has not yet been identified in any MBCs although, the limits established for the water vapor production were found consistent with the observed amount of dust that would be caused by a weak water ice sublimation.

So far, little is known about the Lixiaohua family. Novaković et al. (2010) performed a dynamical analysis of the family and concluded that the evolution of the family is driven by a combination of the Yarkovsky effect, close encounters by large asteroids (e.g. Ceres), and several two- and three-body mean-motion resonances that crosses the family region. These authors estimated the family age in 160 ± 35 Myrs. The only member of the family with an observed spectrum is the largest body, (3330) Gantrisch, classified as an X-type in the Bus taxonomy (Lazzaro et al., 2007; Bus and Binzel, 2002). Masiero et al. (2015), using the NEOWISE data (Mainzer et al., 2016), provided a value of ~ 0.044 for the mean albedo, which suggests a primitive nature for the family. Recently, Morate et al. (2018) performed an analysis based on the near-infrared colors from the MOVIS database (Popescu et al., 2016) of 13 Lixiaohua family members and report that they are probably dominated by primitive asteroids.

In this work we investigate the spectral properties of the Lixiaohua family and the possible link to the main belt comets 311P and 358P. This work is a part of the PRIMitive Asteroid Spectroscopic Survey, an effort to characterize primitive asteroids along the asteroid main-belt. In Section 2, we describe the observation strategy and the sample. The analysis methodology is described in Section 3 with the results for the family spectroscopy presented in Section 4, where we also perform a direct comparison of the investigated properties of the family with the data available for the MBCs. Finally, in Sections 5 and 6, we present the discussion and conclusions.

2. Observation and data reduction

2.1. Visible

We performed low-resolution spectroscopy of 36 asteroids members of the Lixiaohua collisional family. The data was obtained through an observational campaign of eight nights from the first semester 2017 to the first semester of 2018 at the 4.1m SOAR telescope on Cerro-Pachón, Chile.

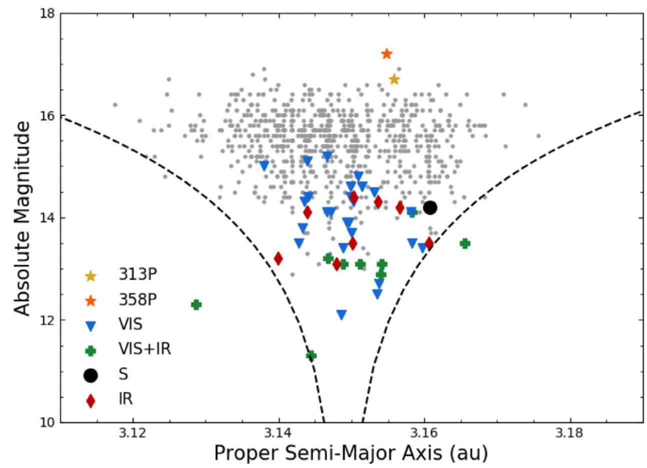

Fig. 1. Absolute Magnitudes of Lixiaohua family asteroids as a function of the semi-major axis (gray circles). Blue triangles indicate members that were observed only in visible wavelengths, while red diamonds indicate the ones obtained only in the near-IR. Purple plus signs show objects observed in both regions. The black solid line represents the Yarkovsky envelope Nesvorný et al. (2015). The brown and yellow stars are MBCS 358P and 313P, respectively, with estimated absolute magnitude obtained from JPL (https://ssd.jpl.nasa.gov/).

We used the Goodman High Throughput Spectrograph (GTHS) with a grating of 400 $lines$/mm and a slit of 1.5ε, with no second order blocking filter (Clemens et al., 2004), which provides a mean resolution of 4000. All observations were made using parallactic angle, and with an astronomical seeing smaller than the slit aperture. Each object was observed in the mode 2 of the grating, which provides a spectrum coverage of 0.5 to 0.9 μm. For the brightest objects (typically $V < 18.5$ mag) on nights with good sky conditions we also observed in the mode 1, which provides a spectrum coverage from 0.4 to 0.7 μm. Hereafter, we will refer to mode 2 as "red-mode" and mode 1 as "blue-mode". This strategy was used because the CCD-camera (red-cam) at the GTHS performs with better quantum efficiency at redder wavelengths. Therefore, faint objects would require too long of an exposure time in "blue-mode". The observation of all objects acquired in both modes were done in a subsequent manner, with the exception of (3556) Lixiaohua that was observed in blue- and red-mode on different nights.

We calibrated the spectra in wavelength using HgNeAr lamps. The reflectance spectrum of the asteroids was obtained by dividing the instrumental flux of the objects with the flux of Solar analogue stars (Landolt, 1992; Colina and Bohlin, 1997) that were acquired at the same night, with similar airmasses. Table A.1 lists the observational conditions of each asteroids in both grating modes and the solar analogues stars that were used to retrieve the reflectance spectrum.

The data was reduced using standard techniques; the images were bias and flat-field corrected using dome flats. In sequence, we extracted the one-dimensional spectrum using variable aperture, according to the SNR of the object and the sky conditions of the night. All of these tasks were accomplished using IRAF and standard Python language libraries, such as Numpy (Van Der Walt et al., 2011), Scipy (Jones et al., 2001), Matplotlib (Hunter, 2007), Pandas (McKinney, 2010) and Astropy (Astropy Collaboration et al., 2013b; Price-Whelan et al., 2018).

2.2. Near-infrared

We observed 17 objects from the Lixiaohua family between May 2016 and October 2018 with the Telescopio Nazionale Galileo (TNG)

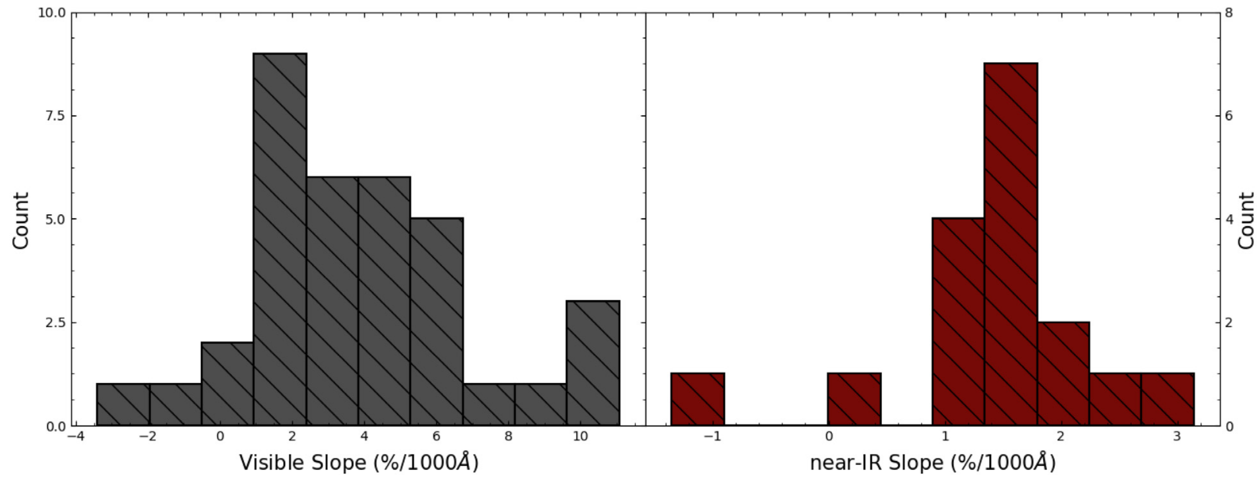

Fig. 2. Visible (*left*) and near-infrared (*right*) slope distribution in the Lixiaohua family.

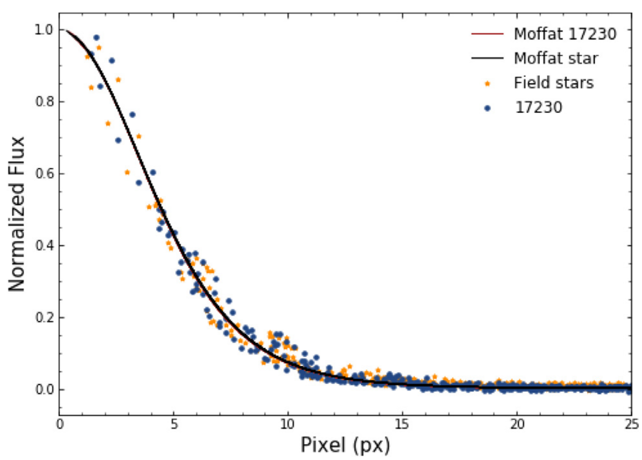

Fig. 3. Result of the PSF analysis of the asteroid (17230) 2000 CX116 (blue) in comparison to star in the same field of view (black). (For interpretation of the references to color in this figure legend, the reader is referred to the web version of this article.)

situated at the Observatory of Roque de Los Muchachos, La Palma, Canary Islands (Spain). We observed them in Director Discretionary Time. We used the Near Infrared Camera Spectrometer (NICS) in spectroscopic mode with the AMICI prism and the 1.5" slit. This setup provides a spectra in the 0.8–2.5 μm range with a resolving power of ∼35 quasi-constant along the spectrum Oliva (2000). During each observation night, we also observed at least two solar analog stars (Landolt, 1992; Colina and Bohlin, 1997) in order to correct for telluric absorptions and to obtain the relative reflectance.

The observations of Lixiaohuas and solar analog stars were performed by moving the objects along the slit by steps of 10 arcsec following a ABBA scheme. The individual exposure times were set at 3–15 s for solar analog stars and 90 s for Lixiaohuas. The ABBA scheme was repeated several times to increase the signal to noise.

We reduced the data following the procedure described in Licandro et al. (2001), using standard IRAF package routines[1] and Python scripts, similar to Section 2.1. First, we subtracted each AB couple of images to remove the sky contribution, and corrected the images obtained or flat field using halogen lamp images taken during the afternoon. Then, we extracted each spectrum obtained from the AB subtractions and averaged them to obtain a single spectrum of each object.

We used our dedicated scripts written in Python programming language, and obtained the reflectance spectra by dividing the spectra of the asteroids by those from the solar analogue stars observed on the same night. The script corrects the results for atmospheric transmission variations, applying sub-pixel offsetting to correct errors in the wavelength calibrations due to instrumental flexures. Finally, we normalized the reflectance at 1.2 μm.

3. Analysis

We present the spectra of 35 asteroids in the visible and 17 in the near-IR. Fig. 1 show the absolute magnitude of the observed targets as a function of semi-major axis. Our strategy was to observe the objects in the maximum wavelength coverage possible, considering that the visible and near infrared data were acquired with telescopes in different hemispheres. The results of the observational campaign are:

- 13 objects observed only in the red-mode (Fig. A.1).
- 13 objects observed in both visible modes, producing a spectrum in the 0.4–0.9 μm range (Fig. A.2).
- 8 objects observed only in the near-infrared (0.9–2.4 μm). These objects were normalized at 1.2 μm (Fig. A.3).
- 3 objects observed in the red-mode and in the near-IR, producing a spectrum coverage of 0.5–2.4 μm (Fig. A.4).
- 6 objects were observed in both visible modes and in the near-IR, producing a spectrum coverage of 0.4–2.4 μm (Fig. A.5).

3.1. Spectroscopic analysis

The analysis of the spectroscopic data was entirely made using the CANA package (De Pra et al., 2018). The sample was characterized through a taxonomical classification and by four parameters that were measured when possible, considering the spectrum wavelength coverage available. These parameters are: visible slope (visible — red-mode), hydration feature (visible — red-mode), turn-off point (visible — blue-mode), and near-IR slope (near-IR).

The visible slope was measured by the angular coefficient in a linear fit to the spectrum using the wavelength range of 0.5–0.9 μm, normalized at 0.55 μm. For the near-IR slope, we used the wavelength

[1] IRAF is distributed by the National Optical Astronomy Observatories, which are operated by the Association of Universities for Research in Astronomy, Inc., under cooperative agreement with the National Science Foundation (Tody, 1986).

Table 1
Results from the analysis of the asteroids spectroscopy. Values marked with '*' means that there was wavelength coverage but feature was not identified. While '–' means that there was not enough wavelength coverage to perform analysis.

Asteroid number	Turn-off point (Å)	Turn-off point error (Å)	Slope visible (%/1000 Å)	Slope visible error (%/1000 Å)	Tax.	Slope Near-IR (%/1000 Å)	Slope Near-IR error (%/1000 Å)
3330	0.5110	0.0010	4.57	0.70	T	3.14	0.67
3556	*	*	6.11	0.65	T	–	–
5771	0.5072	0.0009	2.77	0.71	X	2.58	0.56
5900	–	–	6.64	0.85	T	–	–
16715	–	–	–	–	Xc	1.15	0.66
17230	*	*	2.58	0.61	C	–	–
18477	–	–	–	–	Cg	1.24	0.70
18483	–	–	1.86	0.90	C	0.19	0.51
19862	–	–	–	–	Xk	1.55	0.47
22118	–	–	–	–	Xc	0.97	0.54
25932	*	*	11.00	0.85	D	–	–
26516	–	–	6.79	1.29	L	0.96	0.59
27738	–	–	–	–	Cb	1.54	0.52
34210	–	–	–	–	Cg	1.46	0.75
34228	–	–	2.26	0.65	Xk	–	–
34339	–	–	5.66	0.97	T	–	–
35627	–	–	8.37	0.48	T	1.66	0.66
39094	–	–	0.89	0.92	C	–	–
39260	–	–	–	–	Cb	1.50	0.58
40976	0.5157	0.0067	−1.49	0.67	C	–	–
42089	–	–	10.73	1.33	A	–	–
43152	*	*	5.80	0.82	T	1.83	0.57
44463	*	*	4.82	0.81	X	1.90	0.54
48153	0.5676	0.0053	0.95	0.78	Xc	1.49	0.57
54286	–	–	4.09	0.57	Xe	–	–
56970	–	–	4.48	1.02	Xe	–	–
63312	*	*	3.08	0.65	X	–	–
65264	*	*	2.49	0.43	X	1.49	0.58
66062	–	–	5.48	1.27	T	–	–
71655	–	–	1.53	1.24	Cb	–	–
77495	*	*	1.95	0.86	Xk	–	–
80062	–	–	−0.37	0.56	C	–	–
106085	–	–	5.28	1.02	T	–	–
107861	*	*	2.67	0.53	S	–	–
110518	–	–	3.39	0.55	Xc	–	–
110819	*	*	1.54	0.53	Cg	–	–
123915	*	*	1.52	0.90	Cg	–	–
123979	*	*	11.07	1.35	X	–	–
135384	–	–	1.66	0.55	Cg	–	–
136272	–	–	–	–	B	−1.35	0.64
138668	–	–	1.60	0.75	Xk	–	–
156670	0.5088	0.0042	−3.39	0.87	B	–	–
161079	*	*	3.86	0.86	Xe	–	–

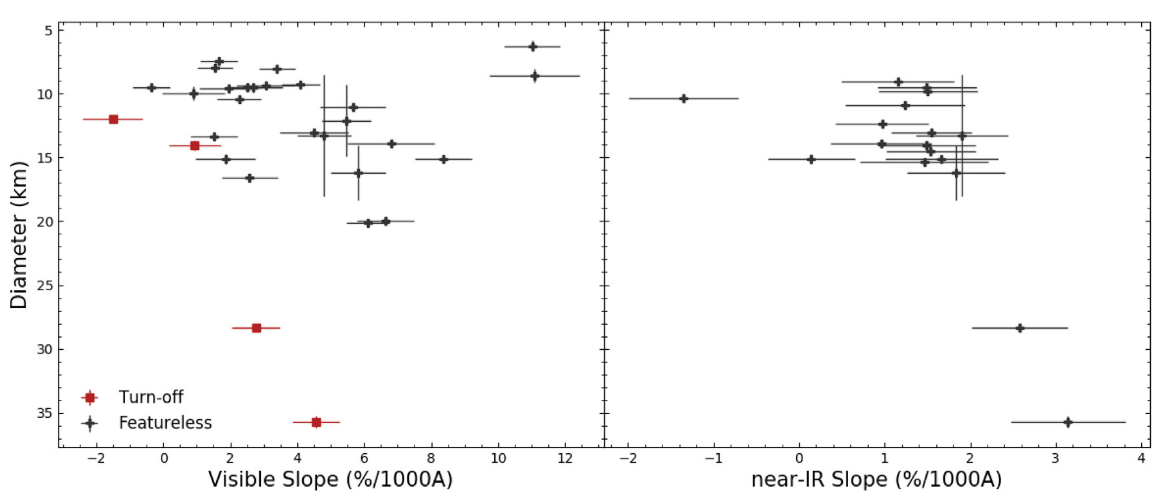

Fig. 4. The distribution of visible slope versus diameter (left) and of near-infrared versus diameter (right). The read dots on the left-side represents object where the turn-off feature was identified.

range of 1.0–2.3 μm, normalized at 1.2 μm. The associated error is the quadratic sum of the systematic error introduced by the solar analogues division, and the error of the fit, estimated by a Monte-Carlo method with a resampling of the reflectance spectra based on the spectrum SNR. Although the results presented ahead are the sum of the described error sources, the systematic error is the strongly dominating term.

We looked for the presence of hydrated minerals through the identification and characterization of an absorption band centered at around 0.7 μm, which is related to the unambiguous indicator near the 3 μm region (see Vilas, 1994; Fornasier et al., 2014; Rivkin et al., 2015). For this task we used the wavelength range of 0.55–0.88 μm. The spectral continuum was estimated by a linear fit within the 0.55–0.57 and 0.84–0.88 μm intervals. Thereafter, we removed the continuum from the spectrum and fit a fourth-order spline in the 0.55–0.88 μm range. We identified the hydration band if the minimum reflectance of the fit is close to 0.7 μm, at a depth higher than 1% and of 3σ of the spectrum signal-to-noise ratio (SNR), where σ is the standard deviation of the spectrum noise.

Another possible indicator of hydration is the presence of the UV turn-off at approximately 0.5 μm. Feierberg et al. (1985) suggested that this feature correlated to the unambiguous indicator of hydration at 3 μm. Vilas (1995) found that the U–B color alone cannot distinguish between differentiated and aqueously altered materials. More recently, Rivkin (2012) reported that the u'-g' color in the Sloan Digital Sky Survey (SDSS) did not differ between the C-complex asteroids with and without a 0.7-μm band. However further studies using spectroscopic data are necessary to assert if the feature is in fact an indicator of hydrated minerals. We measured the presence of this feature using the data available in the 0.4–0.7 μm range, applying the same methodology described in De Prá et al. (2018). We measure the furthest point to a linear fit performed with the edges of the wavelength coverage. To assert the presence of feature, the distance between this point and the fit should surpass a threshold which was defined by trial and error and visual analysis.

The asteroid's taxonomic classification was obtained by the minimization of the chi-squared between the object's spectrum and the templates from the DeMeo et al. (2009) taxonomic system. This procedure was made using the combined spectra with data from all wavelength ranges available. For the objects that were observed only in the visible wavelengths, if the resulting classes does not coexist in the Bus and Binzel (2002) taxonomy, we reclassified it accordingly to the class complex (e.g S_v, would be classified as S).

3.2. Radial profile analysis of 17230

The spectra of (17230) 2000 CX116 presented an unusual increase of reflectance in the near-UV region (Fig. A.2). The object was observed in both visible modes. The coincident wavelength coverage of the two spectra (0.5 to 0.7 μm) presented are self-consistent, suggesting that the behavior at lower wavelengths is real.

Rondón-Briceño et al. (2017) studied the effects of a dust coma in an asteroid spectrum, for impact and sublimation activity drivers. Their model predicts that the dust ejected by the coma would affect the light scattering differently across different wavelengths. One of the outcomes for a weak sublimation-drive activity would be a near-UV increase of reflectance similar to the one observed in this object.

With the theoretical motivation and the fact that this family hosts 2 MBCs, we studied the PSF of the (17230) 2000 CX116, looking for evidence of a weak activity. To determine the presence or not of activity in the asteroids we looked to see the radial profile of the asteroid is widened in comparison to the average radial profile of the stars found in the same field of view (Luu and Jewitt, 1992; Martino et al., 2019). We used the images that were acquired for finding and centering the object in the slit, before observing the target spectrum. The images were dark frame and flat field calibrated. In sequence, we aligned and combined them, using both the coordinates of the stars and the asteroid. Finally, we obtained the object's and stellar radial profile using the *pradprof* routine of the IRAF package. These profiles are normalized and fitted using a Moffat1D of the Astropy library (Astropy Collaboration et al., 2013a).

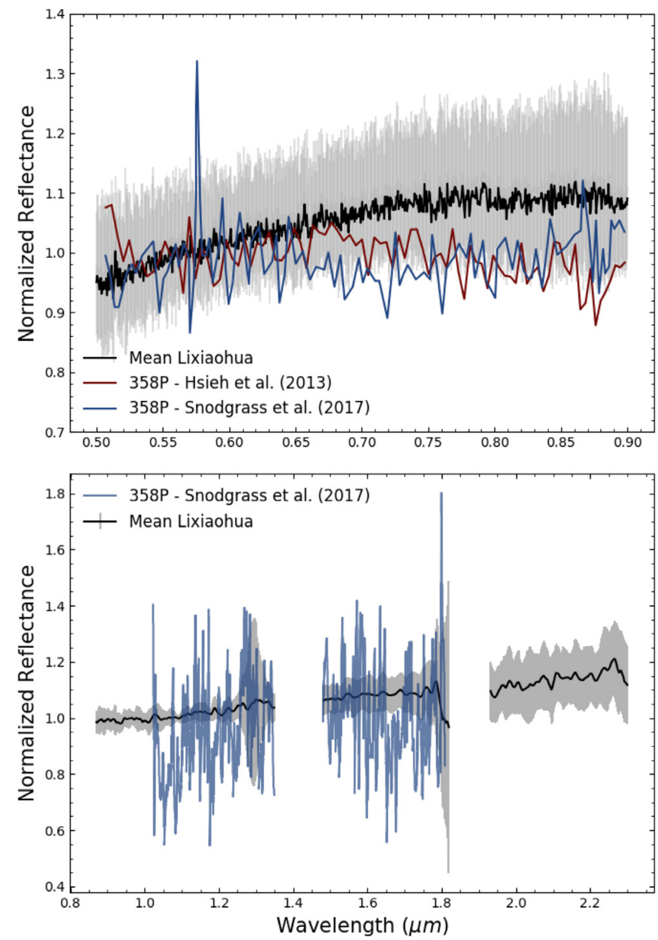

Fig. 5. The mean spectrum of the Lixiaohua family members (black) in comparison with the spectra to the main belt comet 358P obtained by Hsieh et al. (2013) (red) and by Snodgrass et al. (2017) (blue), upper figure in the visible, lower in the near-infrared. The gray region represents the one sigma deviation from the Lixiaohua mean spectrum. We performed a rebinning of the visible spectra of 358P using boxes of 11 Å, for better visualization.

3.3. Public databases

In addition to the spectroscopic data, we extended the analysis gathering data of the Lixiaohua family available from public databases. There were 110 members of the Lixiaohua family listed on the database of SDSS colors provided by Carvano et al. (2010) and Hasselmann et al. (2011). We searched objects on the last release of the MOVIS database (Popescu et al., 2016), that were observed in the Y, K and H filters, and found 24 Lixiaohua members. This choice of filters was based on selecting the highest number of objects that were observed in at least three filters.

We calculated the visible and near-IR spectral slope from the data available in these databases in a way that is compatible with the ones derived from the spectroscopic data. We estimated the angular coefficient from a linear fit using the reflectances on g, r, and i SDSS filters, normalized at 0.55 μm for the visible slope; and using the y, k and h VISTA filters, normalized in 1.2 μm for the near-IR. To calculate the slope uncertainties we created 1000 clones of each observation by drawing random values for the reflectance in each filter using normal distributions with means equal to the listed reflectance value and variances equal to the listed uncertainties. The resultant spectral slope distribution was then fitted with a Gaussian curve, whose mean and variance were then adopted as the nominal value for the spectral slope and its uncertainty, respectively, expressed in units of %/1000 Å. Finally, the mean visible and near-IR slope of the Lixiaohua family was then estimated by a weighted average, using the slope uncertainties as the weights.

4. Results

4.1. Spectroscopic analysis

The results of spectroscopic data analysis are presented in Table 1. The information about the orbital parameters, geometric albedo and diameters are listed in Table A.3. The albedo and diameters were obtained from the latest release of the NEOWISE database (Mainzer et al., 2016).

The Lixiaohua family exhibit a wide variety of visible slopes (Fig. 2), ranging from −3.39 to 11.07%/1000 Å, with a mean value of 3.58%/1000 Å and a standard deviation of 3.21%/1000 Å. In the near-IR there is lower variability, with a mean value of ~ 1.37%/1000 Å and a standard deviation of 0.93%/1000 Å. These values are in good agreement with the ones estimated using the public SDSS and MOVIS databases: 2.79 ± 1.72%/1000 Å and 1.49 ± 2.25%/1000 Å, respectively.

In Fig. 4-*left* we show the distribution of visible slope versus diameter. The larger objects do not deviate considerably from the family mean value, while there is a higher variance in smaller bodies. This behavior was not observed in the near-IR. In fact, the largest objects in the sample presented reddest near-infrared slopes (Fig. 4-*right*).

The taxonomic classification resulted in a majority of the objects belonging in primitive classes, such as the C-complex, X-complex, T- and D-types. Only the object (107861) 2001 FN80 presented a decay of reflectance towards 1 μm, indicating an olivine absorption band, being therefore classified as an S-type. The object (44463) 1998 VT18 also present a drop of reflectance in the visible spectrum, however the feature is not observed in the near-IR, and the overall classification resulted in a X-type. The largest member of the family, (3330) Gantrisch was previously classified as an X-type, based on the visible spectroscopy (Lazzaro et al., 2007). The combined analysis with visible and near-IR data provided a classification as a T-type; an intermediate class between X and D-types, with slopes typically redder than a X-type. The family homonymous asteroid, (3556) Lixiaohua, was also classified as a T-type. It is of note, that some objects which were acquired in both visible and near-IR may present a slight variation in the slope at these wavelengths, such as (26516) 2000 CW56 and (35627) 1998 KW9. However, this behavior is expected since, the visible and near-IR spectra were acquired in different epochs at different phase angles (Lumme and Bowell, 1981; Sanchez et al., 2012).

None of the family members spectra presented an absorption feature at 0.7 μm, suggesting that aqueous alteration did not act strongly on the family. There are four members out of 19 that presented the UV turn-off, including the two largest members. No correlations between the turn-off with any other property was found, except that the other two objects that exhibit the feature are the ones with bluest slopes in the 10–15 km diameter regime (red points in Fig. 4).

4.2. Search for activity in 17230

The analysis of the radial profile of (17230) 2000 CX116 revealed that if activity was present, it could not be detected (Fig. 3). The effect of a coma in the radial profile is highly dependent on the ratio between the mass of coma and the nucleus. The object is considerably large, with an estimated diameter of 16 km, in comparison with the sub-kilometer sized 313P and 328P. Therefore, only a stronger dust emission than the one observed in the MBC members would be detectable in 2000 CX116. Even though the analysis of the PSF was inconclusive, the object spectrum is not well represented by any taxonomic class. The adopted methodology provides a closest resemblance to the C-type class.

4.3. Comparison with the main-belt comets

Only object 358P has published spectra in a wavelength range that is comparable with our observations. In Fig. 5, we show the spectra of 358P obtained by Hsieh et al. (2013) and Snodgrass et al. (2017) in comparison with the average spectra of the Lixiaohua family in both visible and near-IR ranges. The visible spectra obtained by both works are self consistent and bluer than the family mean however, still within the slope dispersion of the family (gray area in Fig. 5). We recalculated the spectral slope for the sake of consistency in the comparison with data acquired by this work, which provides a -1.4 ± 1.0%/1000 Å for Hsieh et al. (2015) and 0.4 ± 2.0%/1000 Å for Snodgrass et al. (2017). These slopes values lie slightly under the one-sigma deviation of the family mean, reported in Section 4. Applying the same methodology as in Section 3, we found no evidence of the 0.7 μm aqueous alteration band or turn-off. The work of Snodgrass et al. (2017) also presented the spectrum of 358P in near-IR, with a slope of 1.36 ± 2.0%/1000 Å, compatible to the family mean.

Unfortunately, there is no available spectrum of 313P at comparable wavelengths for the acquired spectra in this work. Jewitt et al. (2015a) estimated visible slope of 313P is about 5.0 ± 2.0%1000 Å, by the B–V, V–R, B–R colors. The precovery analysis of SDSS images made by Hsieh et al. (2015) and Hui and Jewitt (2015), show that in 2003, the object was active and with mean colors: $g' - r' = 0.54 \pm 0.05$, $r' - i' = 0.10 \pm 0.05$, and $i' - z' = 0.05 \pm 0.05$. These colors provide an estimated slope of 2.2 ± 2.1%1000 Å, using the same methodology as De Prá et al. (2018). Although these estimates were made at slightly different wavelength ranges, both values were normalized at 0.55 μm, comparable to measured values in this work.

5. Discussion

We analyzed visible and near-infrared spectroscopy of members of the Lixiaohua collisional family. Our results show a wide variation of spectral slopes at both wavelengths ranges. Most of the objects where classified as belonging to primitive classes C-, X-complex and D-class, with only one outlier, (107861) 2001 FN80, which belongs to the S-class. Although we found few objects with a turn-off reflectance towards the near-UV, no unambiguous indicator of hydration was found in the visible and near-IR data. Nearly all observed spectra were classified in taxonomic classes compatible with primitive asteroids, with an overall reddish slope both in the visible and in the near-IR.

Comparison with the main-belt comets revealed that the family is slightly redder than 358P in the visible but in good agreement in the near-IR (Hsieh et al., 2013; Snodgrass et al., 2017). In the case of 313P, both color measurements are consistent with the family mean, considering the error bars, although there was variation above one-sigma from colors obtained at different perihelion passages (Hui and Jewitt, 2015; Hsieh et al., 2015; Jewitt et al., 2015a).

Considering the fact that the objects were active when observed, then their slopes were probably contaminated by the presence of the coma. The dust produced by the low-level activity of Main Belt Comets should be dominated by small particles, that are easily ejected from the asteroid. The scattering properties of smaller particles are strongly controlled by their sizes. The model proposed by Rondón-Briceño et al. (2017) suggests that the effect of such coma could increase the near-UV reflectance, while making the visible slope less steep. This behavior would be coupled with an increase of brightness, which is reported on the 358P (Hsieh et al., 2018a), and could explain the bluer slope compared to the family mean. This phenomenon could also have caused the variation of 313P colors. Both Hui and Jewitt (2015) and Hsieh et al. (2015) concluded that 313P was more active in 2003 perihelion passage than the 2014, suggesting that the object was bluer when it was more active.

Even though the coma might be contaminating the slope of the MBCs 358P and 313P, there are objects in the family with similar properties. In particular, there is an increasing spread of visible slope values towards smaller objects (Fig. 4), which is not observed in the near-IR. It is of note that both main belt comets have estimated nucleus of sub-kilometer sizes, considerably below the observed sample in this work. The slope scattering behavior was also observed in different populations such as the Hildas and Cybele populations (De Prá et al., 2018; Gil-Hutton and Brunini, 2008). On an asteroid family this trend can be caused by two main factors: (1) Different surface ages, caused by a variation in the balance of space weathering and collisional resurfacing effects. Larger objects tend to have a saturated surface in terms of environmental effects, while smaller objects are more susceptible to a color variation caused by these effects. A small active object could have a surface more rejuvenated than the inactive larger members of the family. (2) The Lixiaohua family was likely produced by a super-catastrophic disruption (Novaković et al., 2010). Although the parental body may not be differentiated, there could be different layers of materials in the objects' interior, caused by some partial heating in its formation. The break up event could expose materials that went though different geophysical processing. Vernazza et al. (2017) suggested that large P/D-type asteroids could experience different heating processes in their interiors. Therefore, we conclude that the spectra of Lixaouhua family is compatible with the two Main-Belt Comets 313P and 358P.

The Lixiaohua family presents several distinct properties from the Themis family, which is also acknowledged to hold MBC among its members (Hsieh and Jewitt, 2006; Hsieh, 2009; Hsieh et al., 2012; Novaković et al., 2012; Hsieh et al., 2018b). In De Prá et al. (2018), we estimated a mean visible slope of $0.63 \pm 1.64\%/1000$ Å, while Ziffer et al. (2011) estimated an average near-IR slope of $0.12 \pm 0.07\%/1000$ Å for the Themis family. Our results indicates that the Lixiaohua family present an average mean spectrum redder than the Themis in both wavelength ranges. Another dissimilarity is related to the 0.7 μm hydration band; while several works have reported the presence of the feature in members of the Themis family (Florczak et al., 1999; Mothé-Diniz et al., 2005; Fornasier et al., 2014), we found it absent in the Lixiaohua family members. In addition to the hydrated minerals, water ice have been reported on the surface of (24) Themis. In order to explain the presence of ice and hydrated minerals in the Themis family, Marsset et al. (2016) suggested that the parent body had layers that underwent distinct heating. The authors propose that aqueous alteration process could have happened close to the core, while maintaining the ice preserved in the outer layer.

The comparison with Themis families suggests that their parental bodies had different properties. Both families are a probable result of catastrophic collisional events however, from parental bodies with distinct sizes and at different epochs. Durda et al. (2007) estimated the diameter of the Themis parent body in 450 km, while the Lixiaohua was estimated in nearly half of the size, with a diameter of 220 km. The Lixiaohua family is estimated in ~150 Myears (Novaković et al., 2010), while the Themis is an ancient family that was probably formed at nearly 2.5 Gyears (Brož et al., 2013). Therefore, these families could be the result of the break-up of bodies that formed at distinct regions and/or time, and which underwent different thermophysical processing.

The physical properties of the Lixiaohua family, in combination with the occurrence of cometary activity events on two family members, suggest the presence of sub-surface ices. We found no strong indicator of the presence of hydrated minerals, however, observations at the 3 μm region are encouraged to rule out this possibility. The combined properties of the Lixiaohua family suggest that the parental body has undergone nearly no heating since its formation, which indicates an origin close or beyond the snow line.

6. Conclusions

We acquired 35 visible and 17 near-IR spectra of members of the Lixiaohua family. Apart from one object classified as a S-type, all asteroids presented featureless spectra with a mean reddish slope in both wavelength regions. We found few members with a UV turn-off, including the two largest family members, and no unequivocal hydration feature were found. Comparison with the Themis family revealed that the Lixiaohua are averagely redder and with smaller albedo than the prior, which suggests that their parent bodies have undergone distinct thermophysical processing along their history, before the break-up event.

The comparison with main belt comets 313P and 358P showed that they are probably real members of the family, though there could be a process altering their colors due to their coma. Future surveys such as the Large Synoptic Survey Telescope (LSST Science Collaboration, 2009) will enable both targets to be observed close to the aphelion, when the activity should have ceased, allowing the acquisition of nucleus colors. This information will help to understand the link between active asteroids and families, and what processes are acting on them.

Acknowledgments

We thank Henry Hsieh, Bin Yang, and Heather Kaluna for providing the reflectance spectra of 328P/ Panstarrs. M. De Prá acknowledges funding from the Prominent Postdoctoral Program of the University of Central Florida. J. Licandro, and J. de León acknowledge support from the AYA2015-67772-R (MINECO, Spain). JdL acknowledges support from MINECO under the 2015 Severo Ochoa Program SEV-2015-0548. This work is based in part on observations obtained at the Southern Astrophysical Research (SOAR) telescope, which is a joint project of the Ministério da Ciência, Tecnologia, Inovações e Comunicações (MCTIC) do Brasil, the U.S. National Optical Astronomy Observatory (NOAO), the University of North Carolina at Chapel Hill (UNC), and Michigan State University (MSU). This work is partially based on observations made with the Italian Telescopio Nazionale Galileo (TNG) operated on the island of La Palma by the Fundación Galileo Galilei of the INAF (Istituto Nazionale di Astrofisica) at the Spanish Observatorio del Roque de los Muchachos of the Instituto de Astrofisica de Canarias. We thank the director of the Telescopio Nazionale Galileo for allocation of Director's Discretionary Time.

Appendix. Additional figures and tables

See Figs. A.1–A.5 and Tables A.1–A.3.

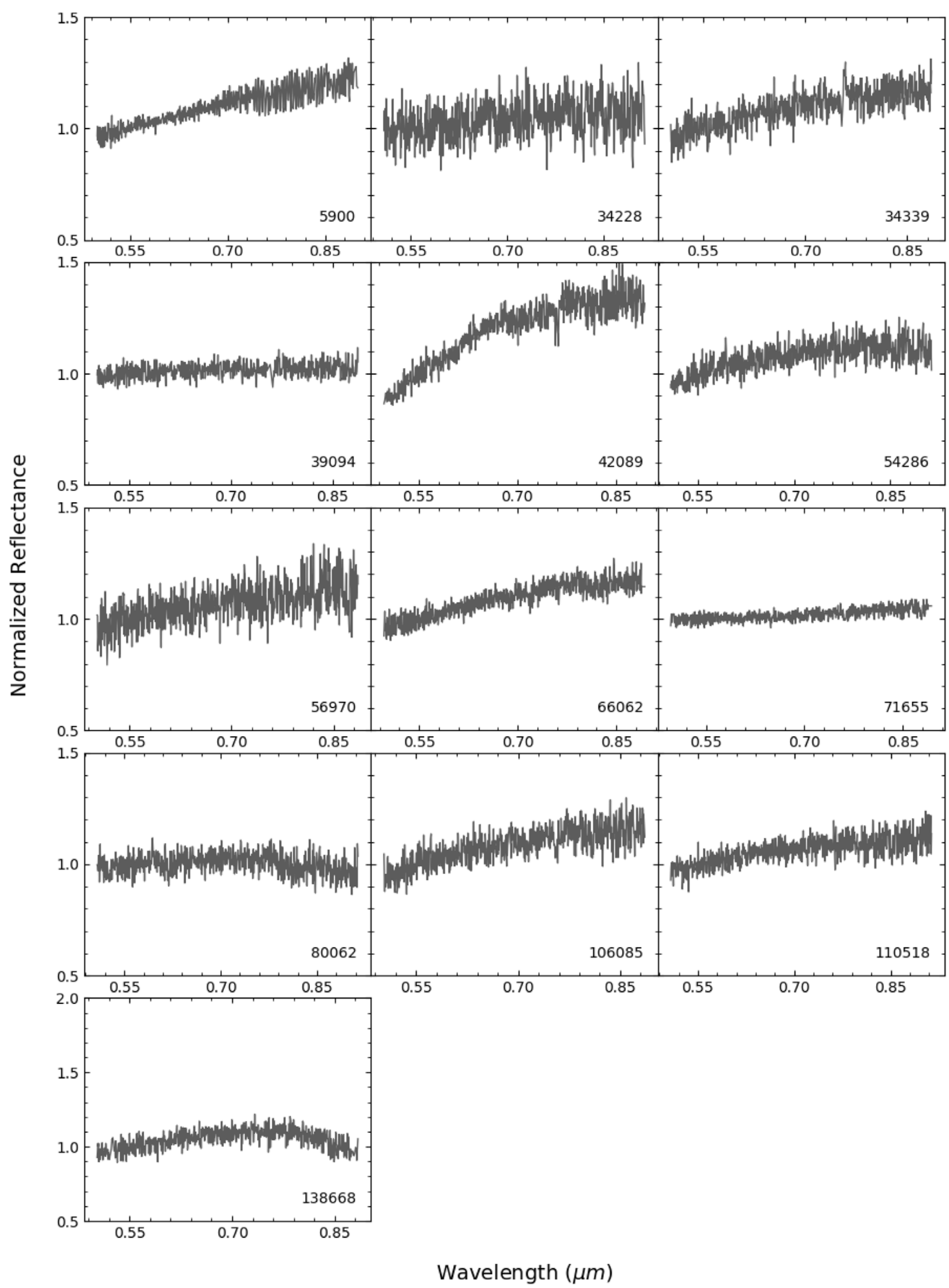

Fig. A.1. Visible spectroscopy in the 0.5–0.9 μm range of asteroids from the Lixiaohua family.

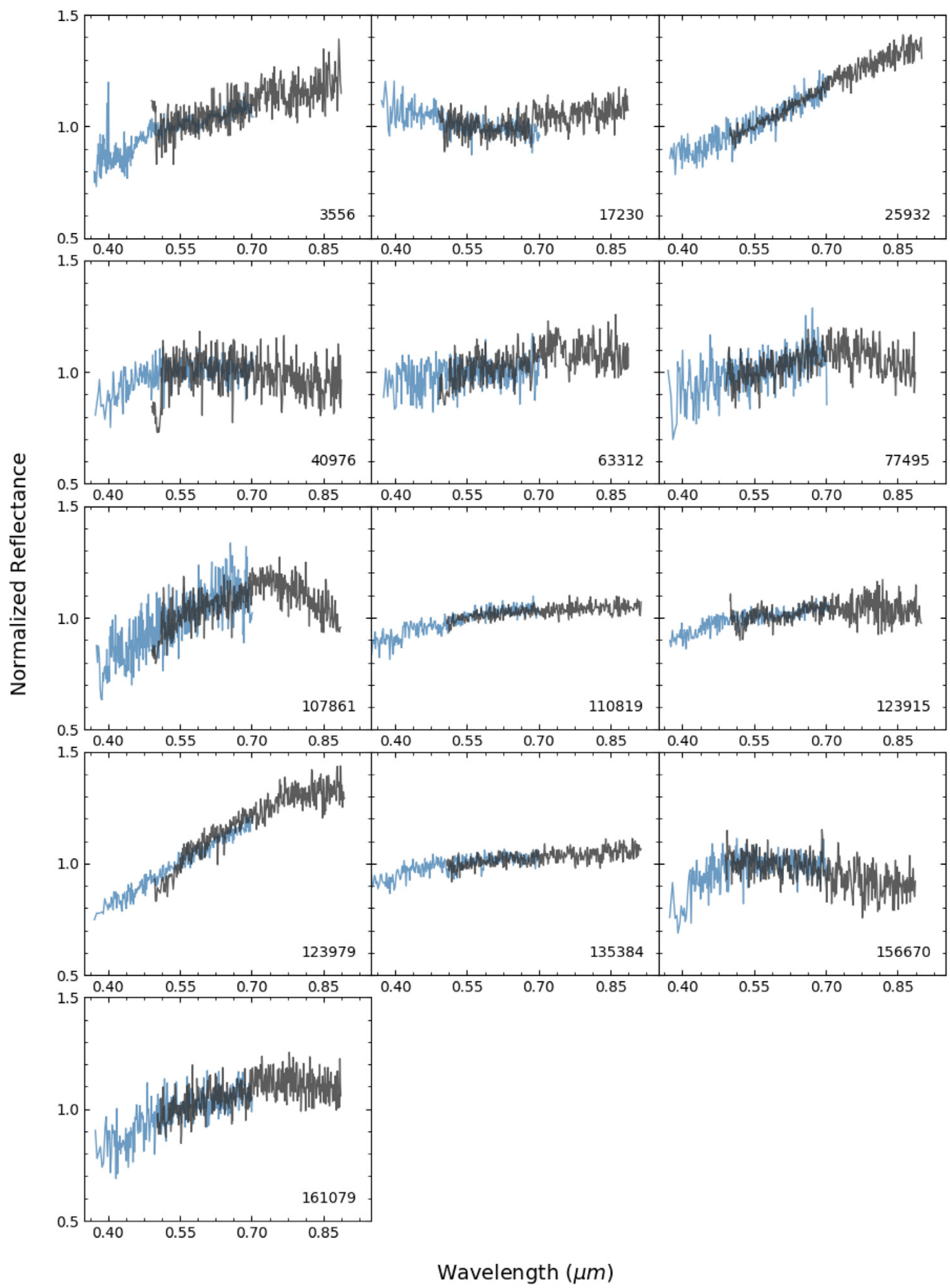

Fig. A.2. Visible spectroscopy in the 0.4–0.7 μm (blue) and 0.5–0.9 μm (gray) of asteroids from the Lixiaohua family. (For interpretation of the references to color in this figure legend, the reader is referred to the web version of this article.)

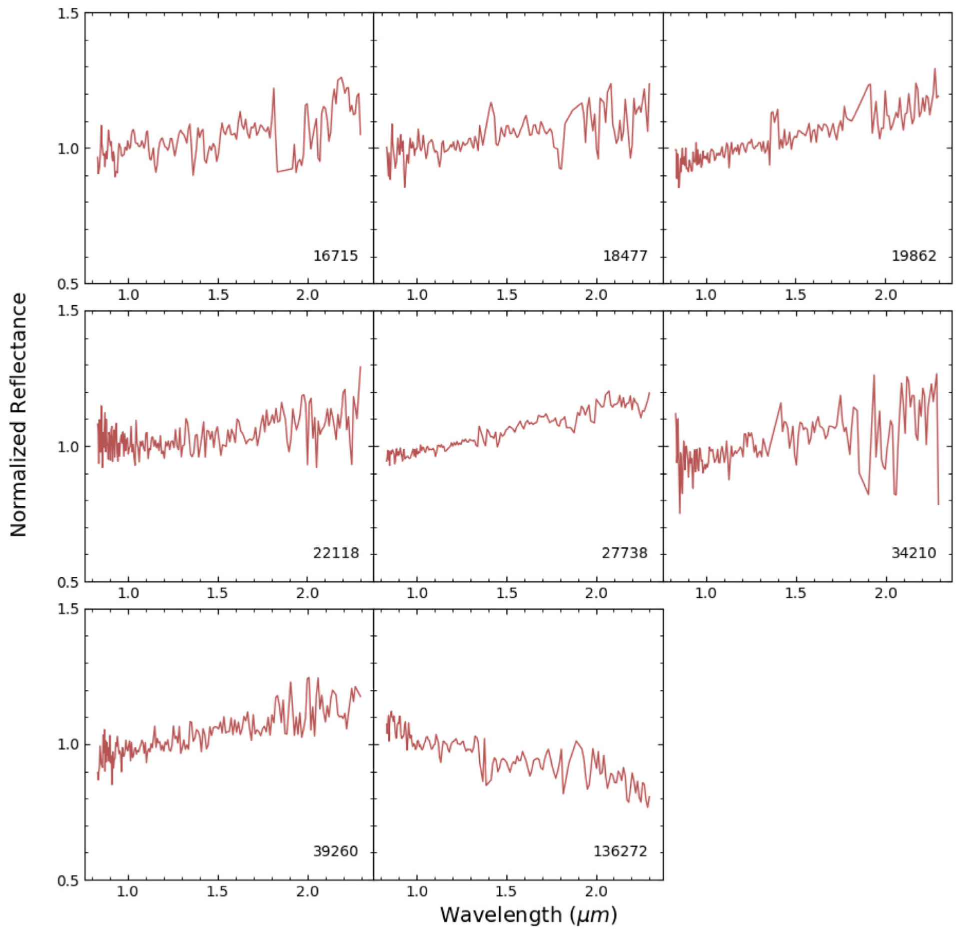

Fig. A.3. Near-IR spectroscopy in the 0.9–2.3 μm range of asteroids from the Lixiaohua family.

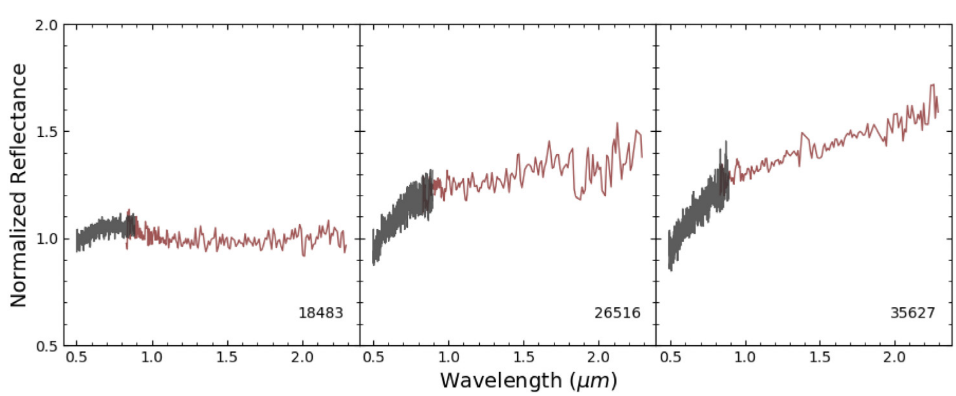

Fig. A.4. Visible spectroscopy in the 0.5–0.9 μm range (gray) and near-IR spectroscopy in the 0.9–2.3 μm (red) range of asteroids from the Lixiaohua family. (For interpretation of the references to color in this figure legend, the reader is referred to the web version of this article.)

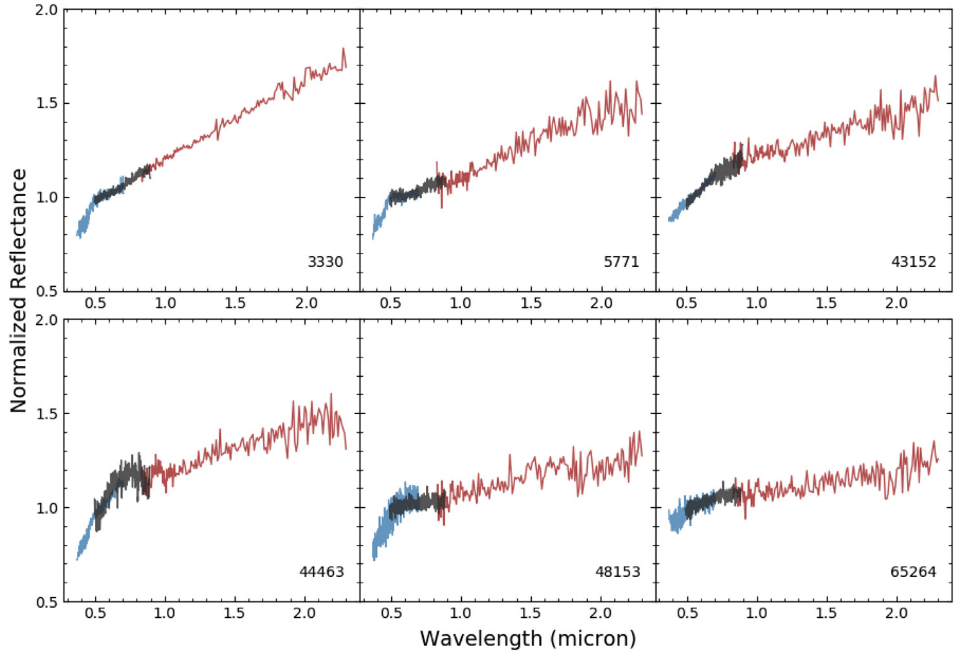

Fig. A.5. Visible spectroscopy in the 0.4–0.7 μm (blue) and 0.5–0.9 μm (gray) and near-IR spectroscopy in the 0.9–2.3 μm (red) range of asteroids from the Lixiaohua family. (For interpretation of the references to color in this figure legend, the reader is referred to the web version of this article.)

Table A.1
Asteroids observational conditions — Visible Spectroscopy.

Asteroid number	Asteroid name	Grating (l/mm)	Mode	Date	Time start (UT)	Airmass	N° Exp	Exp (s)	V (mag)	α (°)	Solar analogs
3330	GANTRISCH	400	m2	2017-02-20	07:44:22	1.07	3	300	17.05	14.55	1,3
–	–	400	m1	2017-02-20	08:03:00	1.06	5	450	19.17	8.74	1,3
3556	LIXIAOHUA	400	m2	2018-03-31	06:24:11	1.04	3	660	18.39	8.22	1,4
–	–	400	m1	2017-02-20	04:57:39	1.15	4	600	18.39	8.22	1,3
5771	SOMERVILLE	400	m2	2017-02-20	03:57:35	1.23	3	300	17.15	2.52	1,3
–	–	400	m1	2017-02-20	04:15:57	1.21	3	450	19.17	8.74	1,3
5900	JENSEN	400	m2	2018-03-09	09:24:35	1.04	3	450	17.82	14.09	1,3
17230	2000 CX116	400	m2	2018-03-31	04:57:56	1.33	3	500	17.74	10.89	1,4
–	–	400	m1	2018-03-31	05:25:21	1.24	3	600	19.17	8.74	1,3
18483	1995 YY2	400	m2	2017-11-18	07:06:13	1.57	3	600	17.78	14.42	2,4,5
25932	2001 DB72	400	m2	2018-03-09	06:46:17	1.20	3	600	18.21	5.26	1,3
–	–	400	m1	2018-03-09	06:02:56	1.16	3	600	19.17	8.74	1,3
26516	2000 CW56	400	m2	2018-03-20	08:28:59	1.10	3	600	18.79	15.46	1,3
27738	1990 TT4	400	m2	2017-07-27	05:12:06	1.14	3	600	17.81	5.75	5,6
34228	2000 QF90	400	m2	2017-07-27	07:40:44	1.25	3	600	18.01	19.78	5,6
34339	2000 QH218	400	m2	2017-11-18	00:55:01	1.27	4	600	18.52	14.39	2,4,5
35627	1998 KW9	400	m2	2018-02-09	01:01:16	1.74	3	600	18.70	11.05	1,2
39094	2000 VQ58	400	m2	2017-11-18	07:54:51	1.45	3	600	18.56	11.92	2,4,5
40976	1999 TV272	400	m2	2018-03-31	00:54:24	1.60	3	600	18.67	21.38	1,4
–	–	400	m1	2018-03-31	00:21:34	1.49	3	600	19.17	8.74	1,3
42089	2001 AQ15	400	m2	2018-03-20	05:00:18	1.44	3	450	18.14	7.67	1,3
43152	1999 XM115	400	m2	2018-03-09	05:08:26	1.16	3	350	16.81	5.77	1,3
–	–	400	m1	2018-03-09	04:42:34	1.13	3	450	19.17	8.74	1,3
44463	1998 VT18	400	m2	2017-02-20	02:34:07	1.41	3	200	17.28	6.37	1,3
–	–	400	m1	2017-02-20	02:51:24	1.34	3	450	19.17	8.74	1,3
48153	2001 FW172	400	m2	2018-04-01	08:33:15	1.08	3	600	18.03	20.78	1,3
–	–	400	m1	2018-04-01	09:11:49	1.05	3	700	19.17	8.74	1,3
54286	2000 JD51	400	m2	2017-07-26	23:54:22	1.23	4	500	18.20	11.69	5,6
56970	2000 SJ111	400	m2	2017-11-18	01:58:36	1.48	3	600	18.62	6.62	2,4,5
63312	2001 FH24	400	m2	2018-03-31	03:53:30	1.08	3	550	18.16	5.55	1,4
–	–	400	m1	2018-03-31	03:21:01	1.15	3	600	19.17	8.74	1,4
65264	2002 GW16	400	m2	2018-02-09	01:45:58	1.36	3	500	17.96	11.34	1,2
–	–	400	m1	2018-02-09	03:56:02	1.35	3	550	19.17	8.74	1,2
66062	1998 RG1	400	m2	2017-02-20	01:34:53	1.40	3	400	17.94	20.08	1,3
71655	2000 EF121	400	m2	2017-02-20	06:48:54	1.22	4	300	17.55	10.17	1,3
77495	2001 HM37	400	m2	2018-04-01	06:53:38	1.38	3	600	19.04	22.37	1,3
–	–	400	m1	2018-04-01	07:28:53	1.20	3	750	19.17	8.74	1,3
80062	1999 JX85	400	m2	2017-07-27	08:54:51	1.10	3	600	18.08	11.96	5,6

(continued on next page)

Table A.1 (*continued*).

Asteroid number	Asteroid name	Grating (l/mm)	Mode	Date	Time start (UT)	Airmass	N° Exp	Exp (s)	V (mag)	α (°)	Solar analogs
106085	2000 SO355	400	m2	2017-11-18	03:49:42	1.80	3	600	18.35	3.47	2,4,5
107861	2001 FN80	400	m2	2018-03-31	08:49:42	1.06	4	600	18.49	15.26	1,4
–	–	400	m1	2018-03-31	08:02:04	1.01	3	600	19.17	8.74	1,4
110518	2001 TY78	400	m2	2017-07-27	01:38:58	1.26	3	550	18.39	6.33	5,6
110819	2001 UW49	400	m2	2017-07-27	06:52:26	1.18	3	600	17.77	5.32	5,6
–	–	400	m1	2017-07-27	06:19:53	1.10	3	600	19.17	8.74	5,6
123915	2001 DK95	400	m2	2018-03-09	07:28:40	1.16	3	550	18.25	7.67	1,3
–	–	400	m1	2018-03-09	08:00:30	1.25	3	550	19.17	8.74	1,3
123979	2001 FB38	400	m2	2018-03-20	07:31:18	1.02	3	500	18.46	13.78	1,3
–	–	400	m1	2018-03-20	06:02:24	1.03	2	600	19.17	8.74	1,3
135384	2001 TT166	400	m2	2017-07-27	02:39:50	1.18	3	500	17.83	2.49	5,6
–	–	400	m1	2017-07-27	03:13:28	1.10	4	600	19.17	8.74	5,6
138668	2000 RB103	400	m2	2017-11-18	02:50:52	1.75	3	500	17.90	3.01	2,4,5
156670	2002 JK111	400	m2	2018-04-01	05:19:31	1.60	3	660	19.21	8.86	1,3
–	–	400	m1	2018-04-01	04:28:26	1.46	3	850	19.17	8.74	1,3
161079	2002 LP61	400	m2	2018-04-01	03:00:48	1.27	2	600	19.17	8.73	1,3
–	–	400	m1	2018-04-01	03:33:24	1.27	3	720	19.17	8.74	1,3

*Solar analogs: (1) Landolt 102–1081, (2) Hyades 64 (3) Landolt 107–978, (4) Landolt 98–978, (5) Landolt 115–271 (6) Landolt 107–684.

Table A.2
Asteroids observational conditions - near-IR.

Asteroid number	Asteroid name	Date	Time start (UT)	Airmass	N° Exp	Exp (s)	V (mag)	α (°)	Solar analogs[a]
3330	GANTRISCH	2017-05-04	01:06:32	1.45	24	90	16.3	7.3	2
5771	SOMERVILLE	2017-02-03	04:43:04	1.75	28	90	17.4	7.0	2,7
16715	TRETTENERO	2016-05-04	04:15:59	1.40	40	90	18.1	3.2	1,2,3,4
18477	1995 WA11	2017-09-08	04:33:02	1.62	32	60	17.9	8.0	5,6
18483	1995 YY2	2017-12-25	23:23:17	1.13	28	90	17.0	0.7	5,6,7
19862	2556 P-L	2016-09-19	04:30:32	1.49	24	90	17.0	6.8	5
22118	2000 SL86	2017-12-25	22:17:00	1.18	32	90	17.2	9.7	5,6,7
26516	2000 CW56	2018-04-28	04:12:14	1.27	32	90	18.1	7.9	3
27738	1990 TT4	2018-10-31	00:24:27	1.27	24	90	16.5	9.0	1,5,6
34210	2000 QV67	2017-09-08	06:00:45	1.22	32	90	17.9	16.1	5,6
35627	1998 KW9	2016-05-04	05:44:01	1.20	33	30	18.2	16.7	5
39260	2000 YE138	2017-12-24	02:45:23	1.12	32	90	17.9	4.4	7
43152	1999 XM115	2017-12-24	06:22:18	1.17	32	90	18.1	20.0	7
44463	1998 VT18	2017-02-03	06:12:17	1.75	30	90	17.6	11.7	2,7
48153	2001 FW172	2018-04-28	05:41:56	1.45	28	90	17.5	16.3	3
65264	2002 GW16	2017-12-24	04:30:04	1.16	32	90	17.9	11.7	7
136272	2003 YF107	2016-05-04	02:20:55	2.10	38	90	18.2	5.3	1,2,3,4

[a]Solar analogs: (1) Landolt 112–1333, (2) Landolt 102–1081, (3) Landolt 107–998, (4) Landolt 110–361, (5) Landolt 93–101, (6) Landolt 115–271, (7) Landolt 98–978.

Table A.3
Orbital and Physical properties of the observed sample.

Asteroid number	Asteroid name	Abs. Mag.	a (au)	e	i (°)	Albedo error	Albedo	Diameter (km)	Diameter error (km)
3330	GANTRISCH	11.3	3.144	0.191	10.45	0.033	0.005	35.717	0.477
3556	LIXIAOHUA	12.7	3.154	0.197	10.15	0.035	0.004	20.085	0.036
5771	SOMERVILLE	12.3	3.129	0.191	10.02	0.029	0.001	28.306	0.264
5900	JENSEN	12.1	3.149	0.191	10.03	0.077	0.023	19.934	0.195
16715	TRETTENERO	14.3	3.154	0.198	10.13	0.041	0.006	9.026	0.157
17230	2000 CX116	12.5	3.153	0.199	10.16	0.077	0.012	16.605	0.311
18477	1995 WA11	14.2	3.157	0.199	10.17	0.045	0.006	10.9	0.09
18483	1995 YY2	13.2	3.147	0.195	10.10	0.102	0.022	15.117	0.4
19862	2556 P-L	13.5	3.161	0.200	10.22	0.047	0.009	13.089	0.099
22118	2000 SL86	13.5	3.150	0.191	10.16	0.055	0.005	12.403	0.16
25932	2001 DB72	14.5	3.153	0.207	10.32	0.065	0.025	6.285	0.425
26516	2000 CW56	13.1	3.149	0.198	10.17	0.063	0.007	13.902	0.324
27738	1990 TT4	13.1	3.148	0.199	10.51	0.048	0.002	14.529	0.15
34210	2000 QV67	13.2	3.140	0.198	10.19	0.052	0.011	15.343	0.094
34228	2000 QF90	13.7	3.150	0.207	10.23	0.064	0.008	10.442	0.185
34339	2000 QH218	13.9	3.150	0.194	10.15	0.053	0.012	11.044	0.196
35627	1998 KW9	12.9	3.154	0.199	10.15	0.065	0.009	15.147	0.061
39094	2000 VQ58	14.1	3.147	0.203	9.95	0.037	0.008	9.994	0.528
39260	2000 YE138	14.1	3.144	0.202	10.30	0.046	0.009	9.824	0.224
40976	1999 TV272	13.5	3.158	0.199	10.13	0.078	0.006	11.972	0.169
42089	2001 AQ15	14.3	3.144	0.198	10.05	–	–	–	–

(*continued on next page*)

Table A.3 (*continued*).

Asteroid number	Asteroid name	Abs. Mag.	a (au)	e	i (°)	Albedo error	Albedo	Diameter (km)	Diameter error (km)
43152	1999 XM115	13.1	3.151	0.204	10.14	0.046	0.013	16.224	2.166
44463	1998 VT18	13.5	3.166	0.200	10.23	0.048	0.032	13.287	4.782
48153	2001 FW172	13.1	3.154	0.199	10.16	0.047	0.01	14.045	0.399
54286	2000 JD51	13.8	3.143	0.202	10.23	0.074	0.015	9.279	0.222
56970	2000 SJ111	13.5	3.143	0.197	10.14	0.024	0.007	13.05	0.112
63312	2001 FH24	13.9	3.149	0.197	10.11	0.061	0.013	9.347	0.312
65264	2002 GW16	14.1	3.158	0.198	10.16	0.045	0.006	9.522	0.312
66062	1998 RG1	13.4	3.160	0.200	10.23	0.08	0.168	12.115	2.794
71655	2000 EF121	13.4	3.149	0.193	10.21	0.052	0.009	13.335	0.152
77495	2001 HM37	14.3	3.150	0.198	10.18	0.048	0.008	9.625	0.147
80062	1999 JX85	14.1	3.158	0.197	10.15	0.041	0.004	9.532	0.12
106085	2000 SO355	15.1	3.144	0.193	10.16	–	–	–	–
107861	2001 FN80	14.2	3.161	0.200	10.22	0.053	0.011	9.559	0.342
110518	2001 TY78	14.6	3.151	0.198	10.16	0.043	0.017	8.041	0.247
110819	2001 UW49	14.4	3.150	0.199	10.16	0.044	0.008	7.971	0.286
123915	2001 DK95	14.1	3.147	0.189	9.98	–	–	–	–
123979	2001 FB38	14.4	3.144	0.196	10.23	0.045	0.012	8.617	0.559
135384	2001 TT166	14.6	3.150	0.202	10.12	0.056	0.008	7.433	0.254
136267	2003 YR80	14.4	3.150	0.200	10.17	0.03	0.003	10.382	0.083
138668	2000 RB103	14.8	3.151	0.191	10.14	–	–	–	–
156670	2002 JK111	15.0	3.138	0.194	10.20	–	–	–	–
161079	2002 LP61	15.2	3.147	0.200	9.85	–	–	–	–

References

Agarwal, J., Mommert, M., 2018. Nucleus of active asteroid 358P/Pan-STARRS (P/2012 T1). Astron. Astrophys. 616, A54. http://dx.doi.org/10.1051/0004-6361/201832761, arXiv:1805.10789.

Astropy Collaboration, Robitaille, T.P., Tollerud, E.J., Greenfield, P., Droettboom, M., Bray, E., Aldcroft, T., Davis, M., Ginsburg, A., Price-Whelan, A.M., 2013a. Astropy: A community python package for astronomy. Astron. Astrophys. 558, A33. http://dx.doi.org/10.1051/0004-6361/201322068, arXiv:1307.6212.

Astropy Collaboration, Robitaille, T.P., Tollerud, E.J., Greenfield, P., Droettboom, M., Bray, E., Aldcroft, T., Davis, M., Ginsburg, A., Price-Whelan, A.M., Kerzendorf, W.E., Conley, A., Crighton, N., Barbary, K., Muna, D., Ferguson, H., Grollier, F., Parikh, M.M., Nair, P.H., Unther, H.M., Deil, C., Woillez, J., Conseil, S., Kramer, R., Turner, J.E.H., Singer, L., Fox, R., Weaver, B.A., Zabalza, V., Edwards, Z.I., Azalee Bostroem, K., Burke, D.J., Casey, A.R., Crawford, S.M., Dencheva, N., Ely, J., Jenness, T., Labrie, K., Lim, P.L., Pierfederici, F., Pontzen, A., Ptak, A., Refsdal, B., Servillat, M., Streicher, O., 2013b. Astropy: A community python package for astronomy. Astron. Astrophys. 558, A33. http://dx.doi.org/10.1051/0004-6361/201322068, arXiv:1307.6212.

Brož, M., Morbidelli, A., Bottke, W.F., Rozehnal, J., Vokrouhlický, D., Nesvorný, D., 2013. Constraining the cometary flux through the asteroid belt during the late heavy bombardment. Astron. Astrophys. 551, A117. http://dx.doi.org/10.1051/0004-6361/201219296, arXiv:1301.6221.

Bus, S.J., Binzel, R.P., 2002. Phase II of the small main-belt asteroid spectroscopic survey. A feature-based taxonomy. Icarus 158, 146–177. http://dx.doi.org/10.1006/icar.2002.6856.

Campins, H., Hargrove, K., Pinilla-Alonso, N., Howell, E.S., Kelley, M.S., Licandro, J., Mothé-Diniz, T., Fernández, Y., Ziffer, J., 2010. Water ice and organics on the surface of the asteroid 24 themis. Nature 464, 1320–1321. http://dx.doi.org/10.1038/nature09029.

Carvano, J.M., Hasselmann, P.H., Lazzaro, D., Mothé-Diniz, T., 2010. SDSS-based taxonomic classification and orbital distribution of main belt asteroids. Astron. Astrophys. 510, A43. http://dx.doi.org/10.1051/0004-6361/200913322.

Clemens, J.C., Crain, J.A., Anderson, R., 2004. The goodman spectrograph. In: Moorwood, A.F.M., Iye, M. (Eds.), Ground-Based Instrumentation for Astronomy. In: Society of Photo-Optical Instrumentation Engineers (SPIE) Conference Series, 5492, pp. 331–340. http://dx.doi.org/10.1117/12.550069.

Colina, L., Bohlin, R., 1997. Absolute flux distributions of solar analogs from the UV to the near-IR. Astron. J. 113, 1138–1144. http://dx.doi.org/10.1086/118332.

De Pra, M.N., Carvano, J., Morate, D., Pinilla-Alonso, N., Licandro, J., 2018. CANA: A python package for the analysis of hydration in asteroid spectroscopic and spectrophotometric data. In: AAS/Division for Planetary Sciences Meeting Abstracts. p. 315.02.

De Prá, M.N., Pinilla-Alonso, N., Carvano, J.M., Licandro, J., Campins, H., Mothé-Diniz, T., De León, J., Alí-Lagoa, V., 2018. PRIMASS visits hilda and cybele groups. Icarus 311, 35–51. http://dx.doi.org/10.1016/j.icarus.2017.11.012, arXiv:1711.02071.

DeMeo, F.E., Binzel, R.P., Slivan, S.M., Bus, S.J., 2009. An extension of the bus asteroid taxonomy into the near-infrared. Icarus 202, 160–180. http://dx.doi.org/10.1016/j.icarus.2009.02.005.

Durda, D.D., Bottke, W.F., Nesvorný, D., Enke, B.L., Merline, W.J., Asphaug, E., Richardson, D.C., 2007. Size-frequency distributions of fragments from SPH/ N-body simulations of asteroid impacts: Comparison with observed asteroid families. Icarus 186 (2), 498–516. http://dx.doi.org/10.1016/j.icarus.2006.09.013.

Feierberg, M.A., Lebofsky, L.A., Tholen, D.J., 1985. The nature of c-class asteroids from 3-μm spectrophotometry. Icarus 63 (2), 183–191. http://dx.doi.org/10.1016/0019-1035(85)90002-8.

Florczak, M., Lazzaro, D., Mothé-Diniz, T., Angeli, C.A., Betzler, A.S., 1999. A spectroscopic study of the THEMIS family. Astron. Astrophys. Suppl. Ser. 134, 463–471. http://dx.doi.org/10.1051/aas:1999150.

Fornasier, S., Lantz, C., Barucci, M.A., Lazzarin, M., 2014. Aqueous alteration on main belt primitive asteroids: Results from visible spectroscopy. Icarus 233, 163–178. http://dx.doi.org/10.1016/j.icarus.2014.01.040, arXiv:1402.0175.

Gil-Hutton, R., Brunini, A., 2008. Surface composition of hilda asteroids from the analysis of the sloan digital sky survey colors. Icarus 193 (2), 567–571.

Haghighipour, N., 2009. Dynamical constraints on the origin of main belt comets. Meteorit. Planet. Sci. 44, 1863–1869. http://dx.doi.org/10.1111/j.1945-5100.2009.tb01995.x, arXiv:0910.5746.

Hasselmann, P.H., Carvano, J.M., Lazzaro, D., 2011. SDSS-based asteroid taxonomy V1.0. NASA Planet. Data Syst. 145.

Hsieh, H.H., 2009. The hawaii trails project: Comet-hunting in the main asteroid belt. Astron. Astrophys. 505 (3), 1297–1310. http://dx.doi.org/10.1051/0004-6361/200912342, arXiv:0907.5505.

Hsieh, H.H., Haghighipour, N., 2016. Potential jupiter-family comet contamination of the main asteroid belt. Icarus 277, 19–38. http://dx.doi.org/10.1016/j.icarus.2016.04.043, arXiv:1604.08557.

Hsieh, H.H., Hainaut, O., Novaković, B., Bolin, B., Denneau, L., Fitzsimmons, A., Haghighipour, N., Kleyna, J., Kokotanekova, R., Lacerda, P., Meech, K.J., Micheli, M., Moskovitz, N., Schunova, E., Snodgrass, C., Wainscoat, R.J., Wasserman, L., Waszczak, A., 2015. Sublimation-driven activity in main-belt comet 313p/gibbs. Astrophys. J. 800, L16. http://dx.doi.org/10.1088/2041-8205/800/1/L16, arXiv:1501.03873.

Hsieh, H.H., Ishiguro, M., Knight, M.M., Micheli, M., Moskovitz, N.A., Sheppard, S.S., Trujillo, C.A., 2018a. The reactivation and nucleus characterization of main-belt comet 358p/PANSTARRS (P/2012 T1). Astron. J. 156, 39. http://dx.doi.org/10.3847/1538-3881/aac81c, arXiv:1805.09353.

Hsieh, H.H., Jewitt, D., 2006. A population of comets in the main asteroid belt. Science 312 (5773), 561–563. http://dx.doi.org/10.1126/science.1125150.

Hsieh, H.H., Kaluna, H.M., Novaković, B., Yang, B., Haghighipour, N., Micheli, M., Denneau, L., Fitzsimmons, A., Jedicke, R., Kleyna, J., Vereš, P., Wainscoat, R.J., Ansdell, M., Elliott, G.T., Keane, J.V., Meech, K.J., Moskovitz, N.A., Riesen, T.E., Sheppard, S.S., Sonnett, S., Tholen, D.J., Urban, L., Kaiser, N., Chambers, K.C., Burgett, W.S., Magnier, E.A., Morgan, J.S., Price, P.A., 2013. Main-belt comet P/2012 T1 (PANSTARRS). Astrophys. J. 771, L1. http://dx.doi.org/10.1088/2041-8205/771/1/L1, arXiv:1305.5558.

Hsieh, H.H., Novaković, B., Kim, Y., Brasser, R., 2018b. Asteroid family associations of active asteroids. Astron. J. 155, 96. http://dx.doi.org/10.3847/1538-3881/aaa5a2, arXiv:1801.01152.

Hsieh, H.H., Yang, B., Haghighipour, N., Kaluna, H.M., Fitzsimmons, A., Denneau, L., Novaković, B., Jedicke, R., Wainscoat, R.J., Armstrong, J.D., Duddy, S.R., Lowry, S.C., Trujillo, C.A., Micheli, M., Keane, J.V., Urban, L., Riesen, T., Meech, K.J., Abe, S., Cheng, Y.-C., Chen, W.-P., Granvik, M., Grav, T., Ip, W.-H., Kinoshita, D., Kleyna, J., Lacerda, P., Lister, T., Milani, A., Tholen, D.J., Vereš, P., Lisse, C.M., Kelley, M.S., Fernández, Y.R., Bhatt, B.C., Sahu, D.K., Kaiser, N., Chambers, K.C., Hodapp, K.W., Magnier, E.A., Price, P.A., Tonry, J.L., 2012. Discovery of main-belt comet P/2006 VW_{139} by Pan-STARRS1. Astrophys. J. 748 (1), L15. http://dx.doi.org/10.1088/2041-8205/748/1/L15, arXiv:1202.2126.

Hui, M.-T., Jewitt, D., 2015. Archival observations of active asteroid 313p/Gibbs. Astron. J. 149 (4), 134. http://dx.doi.org/10.1088/0004-6256/149/4/134.

Hunter, J.D., 2007. Matplotlib: A 2d graphics environment. Comput. Sci. Eng. 9 (3), 90.

Jewitt, D., 2012. The active asteroids. Astron. J. 143, 66. http://dx.doi.org/10.1088/0004-6256/143/3/66, arXiv:1112.5220.

Jewitt, D., Agarwal, J., Peixinho, N., Weaver, H., Mutchler, M., Hui, M.-T., Li, J., Larson, S., 2015a. A new active asteroid 313p/gibbs. Astron. J. 149, 81. http://dx.doi.org/10.1088/0004-6256/149/2/81, arXiv:1412.6582.

Jewitt, D., Hsieh, H., Agarwal, J., 2015b. The active asteroids. In: IV, A., Michel, P., DeMeo, F.E., Bottke, W.F. (Eds.), University of Arizona Press, Tucson, pp. 221–241. http://dx.doi.org/10.2458/azu_uapress_9780816532131-ch012, 895 Pp.

Jones, E., Oliphant, T., Peterson, P., et al., 2001. Scipy: Open source scientific tools for Python. http://www.scipy.org/. [Online; accessed <today>].

Landolt, A.U., 1992. UBVRI photometric standard stars in the magnitude range 11.5 < V < 16.0 around the celestial equator. Astron. J. 104, 340. http://dx.doi.org/10.1086/116242.

Lazzaro, D., Angeli, C.A., Carvano, J.M., Mothe-Diniz, T., Duffard, R., Florczak, M., 2007. Small solar system objects spectroscopic survey V1.0. NASA Planet. Data Syst. EAR–A–I0052–8–S3OS2–V1.0.

Licandro, J., Campins, H., Kelley, M., Hargrove, K., Pinilla-Alonso, N., Cruikshank, D., Rivkin, A.S., Emery, J., 2011. (65) Cybele: Detection of small silicate grains, water-ice, and organics. Astron. Astrophys. 525, A34. http://dx.doi.org/10.1051/0004-6361/201015339.

Licandro, J., Oliva, E., Di Martino, M., 2001. NICS-TNG infrared spectroscopy of trans-neptunian objects 2000 EB173 and 2000 WR106. Astron. Astrophys. 373, L29–L32. http://dx.doi.org/10.1051/0004-6361:20010758, arXiv:astro-ph/0105434.

LSST Science Collaboration, 2009. LSST science book, version 2.0. ArXiv:0912.0201.

Lumme, K., Bowell, E., 1981. Radiative transfer in the surfaces of atmosphereless bodies. I. Theory. Astron. J. 86, 1694–1721. http://dx.doi.org/10.1086/113054.

Luu, J.X., Jewitt, D.C., 1992. Near-aphelion CCD photometry of comet P/Schwassmann-Wachmann 2. Astron. J. 104, 2243. http://dx.doi.org/10.1086/116400.

Mainzer, A.K., Bauer, J.M., Cutri, R.M., Grav, T., Kramer, E.A., Masiero, J.R., Nugent, C.R., Sonnett, S.M., Stevenson, R.A., Wright, E.L., 2016. NEOWISE diameters and albedos V1.0. NASA Planet. Data Syst. 247.

Marsset, M., Vernazza, P., Birlan, M., DeMeo, F., Binzel, R.P., Dumas, C., Milli, J., Popescu, M., 2016. Compositional characterisation of the themis family. Astron. Astrophys. 586, A15. http://dx.doi.org/10.1051/0004-6361/201526962, arXiv:1601.02405.

Martino, S., Tancredi, G., Monteiro, F., Lazzaro, D., Rodrigues, T., 2019. Monitoring of asteroids in cometary orbits and active asteroids. Planet. Space Sci. 166, 135–148. http://dx.doi.org/10.1016/j.pss.2018.09.001.

Masiero, J.R., DeMeo, F.E., Kasuga, T., Parker, A.H., 2015. In: IV, A., Michel, P., DeMeo, F.E., Bottke, W.F. (Eds.), Asteroid Family Physical Properties. University of Arizona Press, Tucson, pp. 323–340. http://dx.doi.org/10.2458/azu_uapress_9780816532131-ch017.

McKinney, W., 2010. Data structures for statistical computing in python. In: van der Walt, S. and Millman, J., Proceedings of the 9th Python in Science Conference. pp. 51–56.

Morate, D., Licandro, J., Popescu, M., de León, J., 2018. Color study of asteroid families within the MOVIS catalog. Astron. Astrophys. 617, A72. http://dx.doi.org/10.1051/0004-6361/201832780.

Morbidelli, A., Chambers, J., Lunine, J.I., Petit, J.M., Robert, F., Valsecchi, G.B., Cyr, K.E., 2000. Source regions and time scales for the delivery of water to earth. Meteorit. Planet. Sci. 35, 1309–1320. http://dx.doi.org/10.1111/j.1945-5100.2000.tb01518.x.

Moreno, F., Cabrera-Lavers, A., Vaduvescu, O., Licand ro, J., Pozuelos, F., 2013. The dust environment of main-belt comet p/2012 T1 (PANSTARRS). Astrophys. J. 770 (2), L30. http://dx.doi.org/10.1088/2041-8205/770/2/L30, arXiv:1305.4380.

Mothé-Diniz, T., Roig, F., Carvano, J.M., 2005. Reanalysis of asteroid families structure through visible spectroscopy. Icarus 174 (1), 54–80. http://dx.doi.org/10.1016/j.icarus.2004.10.002.

Nesvorný, D., Brož, M., Carruba, V., 2015. Identification and dynamical properties of asteroid families. In: IV, A., Michel, P., DeMeo, F.E., Bottke, W.F. (Eds.), University of Arizona Press, Tucson, pp. 297–321. http://dx.doi.org/10.2458/azu_uapress_9780816532131-ch016, 895 Pp.

Novaković, B., Hsieh, H.H., Cellino, A., 2012. P/2006 VW_{139}: A main-belt comet born in an asteroid collision?. Mon. Not. R. Astron. Soc. 424 (2), 1432–1441. http://dx.doi.org/10.1111/j.1365-2966.2012.21329.x, arXiv:1205.4949.

Novaković, B., Tsiganis, K., Knežević, Z., 2010. Dynamical portrait of the lixiaohua asteroid family. Celestial Mech. Dynam. Astronom. 107 (1–2), 35–49. http://dx.doi.org/10.1007/s10569-010-9263-9.

Oliva, E., 2000. Infrared instrumentation for large telescopes : An alternative approach. Mem. Soc. Astron. Ital. 71, 861, arXiv:astro-ph/9909108.

O'Rourke, L., Snodgrass, C., de Val-Borro, M., Biver, N., Bockelée-Morvan, D., Hsieh, H., Teyssier, D., Fernandez, Y., Kueppers, M., Micheli, M., Hartogh, P., 2013. Determination of an upper limit for the water outgassing rate of main-belt comet P/2012 T1 (PANSTARRS). Astrophys. J. 774 (1), L13. http://dx.doi.org/10.1088/2041-8205/774/1/L13.

Platz, T., Nathues, A., Schorghofer, N., Preusker, F., Mazarico, E., Schröder, S.E., Byrne, S., Kneissl, T., Schmedemann, N., Combe, J.P., 2016. Surface water-ice deposits in the northern shadowed regions of ceres. Nat. Astron. 1, 0007. http://dx.doi.org/10.1038/s41550-016-0007.

Popescu, M., Licandro, J., Morate, D., de León, J., Nedelcu, D.A., Rebolo, R., McMahon, R.G., Gonzalez-Solares, E., Irwin, M., 2016. Near-infrared colors of minor planets recovered from VISTA-VHS survey (MOVIS). Astron. Astrophys. 591, A115. http://dx.doi.org/10.1051/0004-6361/201628163, arXiv:1605.05594.

Price-Whelan, A.M., Sipőcz, B.M., Günther, H.M., Lim, P.L., Crawford, S.M., Conseil, S., Shupe, D.L., Craig, M.W., Dencheva, N., Ginsburg, A., VanderPlas, J.T., Bradley, L.D., Pérez-Suárez, D., de Val-Borro, M., Paper Contributors, P., Aldcroft, T.L., Cruz, K.L., Robitaille, T.P., Tollerud, E.J., Coordination Committee, A., Ardelean, C., Babej, T., Bach, Y.P., Bachetti, M., Bakanov, A.V., Bamford, S.P., Barentsen, G., Barmby, P., Baumbach, A., Berry, K.L., Biscani, F., Boquien, M., Bostroem, K.A., Bouma, L.G., Brammer, G.B., Bray, E.M., Breytenbach, H., Buddelmeijer, H., Burke, D.J., Calderone, G., Cano Rodríguez, J.L., Cara, M., Cardoso, J.V.M., Cheedella, S., Copin, Y., Corrales, L., Crichton, D., D'Avella, D., Deil, C., Depagne, É., Dietrich, J.P., Donath, A., Droettboom, M., Earl, N., Erben, T., Fabbro, S., Ferreira, L.A., Finethy, T., Fox, R.T., Garrison, L.H., Gibbons, S.L.J., Goldstein, D.A., Gommers, R., Greco, J.P., Greenfield, P., Groener, A.M., Grollier, F., Hagen, A., Hirst, P., Homeier, D., Horton, A.J., Hosseinzadeh, G., Hu, L., Hunkeler, J.S., Ivezić, Ž., Jain, A., Jenness, T., Kanarek, G., Kendrew, S., Kern, N.S., Kerzendorf, W.E., Khvalko, A., King, J., Kirkby, D., Kulkarni, A.M., Kumar, A., Lee, A., Lenz, D., Littlefair, S.P., Ma, Z., Macleod, D.M., Mastropietro, M., McCully, C., Montagnac, S., Morris, B.M., Mueller, M., Mumford, S.J., Muna, D., Murphy, N.A., Nelson, S., Nguyen, G.H., Ninan, J.P., Nöthe, M., Ogaz, S., Oh, S., Parejko, J.K., Parley, N., Pascual, S., Patil, R., Patil, A.A., Plunkett, A.L., Prochaska, J.X., Rastogi, T., Reddy Janga, V., Sabater, J., Sakurikar, P., Seifert, M., Sherbert, L.E., Sherwood-Taylor, H., Shih, A.Y., Sick, J., Silbiger, M.T., Singanamalla, S., Singer, L.P., Sladen, P.H., Sooley, K.A., Sornarajah, S., Streicher, O., Teuben, P., Thomas, S.W., Tremblay, G.R., Turner, J.E.H., Terrón, V., van Kerkwijk, M.H., de la Vega, A., Watkins, L.L., Weaver, B.A., Whitmore, J.B., Woillez, J., Zabalza, V., Contributors, A., 2018. The astropy project: Building an open-science project and status of the v2.0 core package. Astron. J. 156, 123. http://dx.doi.org/10.3847/1538-3881/aabc4f.

Rivkin, A.S., 2012. The fraction of hydrated c-complex asteroids in the asteroid belt from SDSS data. Icarus 221 (2), 744–752. http://dx.doi.org/10.1016/j.icarus.2012.08.042.

Rivkin, A.S., Campins, H., Emery, J.P., Howell, E.S., Licandro, J., Takir, D., Vilas, F., 2015. Astronomical observations of volatiles on asteroids. In: IV, A., Michel, P., DeMeo, F.E., Bottke, W.F. (Eds.), University of Arizona Press, Tucson, pp. 65–87. http://dx.doi.org/10.2458/azu_uapress_9780816532131-ch004, 895 Pp..

Rivkin, A.S., Emery, J.P., 2010. Detection of ice and organics on an asteroidal surface. Nature 464, 1322–1323. http://dx.doi.org/10.1038/nature09028.

Rondón-Briceño, E., Carvano, J.M., Lorenz-Martins, S., 2017. A study of the effects of faint dust comae on the spectra of asteroids. Mon. Not. R. Astron. Soc. 468, 1556–1566. http://dx.doi.org/10.1093/mnras/stx536.

Sanchez, J.A., Reddy, V., Nathues, A., Cloutis, E.A., Mann, P., Hiesinger, H., 2012. Phase reddening on near-earth asteroids: Implications for mineralogical analysis, space weathering and taxonomic classification. Icarus 220 (1), 36–50. http://dx.doi.org/10.1016/j.icarus.2012.04.008, arXiv:1205.0248.

Snodgrass, C., Yang, B., Fitzsimmons, A., 2017. X-shooter search for outgassing from main belt comet P/2012 T1 (Pan-STARRS). Astron. Astrophys. 605, A56. http://dx.doi.org/10.1051/0004-6361/201731085, arXiv:1706.06760.

Tody, D., 1986. The IRAF data reduction and analysis system. In: Crawford, D.L. (Ed.), Proc. SPIE. In: Society of Photo-Optical Instrumentation Engineers (SPIE) Conference Series, 627, p. 733. http://dx.doi.org/10.1117/12.968154.

Van Der Walt, S., Colbert, S., Varoquaux, G., 2011. The numpy array: A structure for efficient numerical computation. Comput. Sci. Eng. 13 (2), 22.

Vernazza, P., Castillo-Rogez, J., Beck, P., Emery, J., Brunetto, R., Delbo, M., Marsset, M., Marchis, F., Groussin, O., Zanda, B., Lamy, P., Jorda, L., Mousis, O., Delsanti, A., Djouadi, Z., Dionnet, Z., Borondics, F., Carry, B., 2017. Different origins or different evolutions? decoding the spectral diversity among c-type asteroids. Astron. J. 153 (2), 72. http://dx.doi.org/10.3847/1538-3881/153/2/72, arXiv:1701.06603.

Vilas, F., 1994. A cheaper, faster, better way to detect water of hydration on solar system bodies. Icarus 111 (2), 456–467. http://dx.doi.org/10.1006/icar.1994.1156.

Vilas, F., 1995. Is the U-B color sufficient for identifying water of hydration on solar system bodies? Icarus 115, 217–218. http://dx.doi.org/10.1006/icar.1995.1092.

Ziffer, J., Campins, H., Licandro, J., Walker, M.E., Fernandez, Y., Clark, B.E., Mothe-Diniz, T., Howell, E., Deshpande, R., 2011. Near-infrared spectroscopy of primitive asteroid families. Icarus 213 (2), 538–546. http://dx.doi.org/10.1016/j.icarus.2011.04.008.